Hierarchical Porous and High Surface Area Tubular Carbon as Dye Adsorbent and Capacitor Electrode

Long Chen, Tuo Ji, Logan Brisbin, and Jiahua Zhu*

Intelligent Composites Laboratory, Department of Chemical and Biomolecular Engineering, The University of Akron, Akron, Ohio 44325, United States

S *Supporting Information*

ABSTRACT: Hierarchically porous tubular carbon (HPTC) with large surface area of 1094 m^2/g has been successfully synthesized by selectively removing lignin from natural wood. No templates or chemicals are involved during the process. By further KOH activation, surface area of activated HPTC reaches up to 2925 m^2/g. These materials show unprecedented high adsorption capacity toward organic dyes (methylene blue, 838 mg/g; methyl orange, 264 mg/g) and large electrochemical capacitance of >200 F/g. The sustainable feature of the wood precursor and demonstrated superior adsorption and energy storage properties allow promising applications of the processed materials in energy and environmental related fields.

KEYWORDS: biomass, mesoporous materials, hierarchical structure, environmental chemistry, energy storage
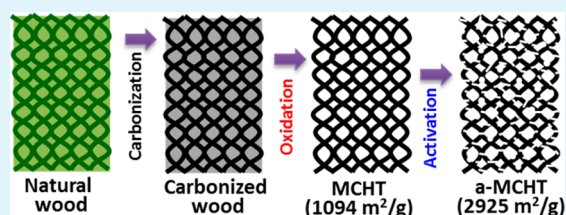
INTRODUCTION

The tunable pore structure in porous carbon materials makes them ideal candidates in versatile applications such as adsorption and separation, catalysis, energy storage/conversion, and electrochemical sensors.[1−10] When rapid diffusion of molecules into porous carbon internal surface is required, especially in adsorption and catalytic reactions, materials possessing mesopores are desirable. Conventionally, mesoporous carbon (MC) is synthesized by nanocasting or a hard-template method,[11−18] where carbon precursor is introduced into the pores of the ordered mesoporous silicas by impregnation, followed by in situ carbonization and removal of the silica template. This hard-templating method is time-consuming, costly, and unsuitable for scale-up production. In particular, the necessity of removing the inorganic template by employing hazardous chemicals such as HF and NaOH is an unavoidable drawback. Alternatively, direct soft-templating[13,19−23] of the carbon material has been developed to prepare MC, which avoids the usage of hazardous chemicals employed for template removal. Soft-template method involves the cooperative assembly of structure-directing agents that are able to form lyotropic phases with suitable organic carbon precursors. Since the first successful synthesis of ordered MC by soft-templating with amphiphilic block copolymers, reported by Dai and co-workers in 2004,[24] extensive research has been conducted to fabricate different pore structures, including but not limited to *p6mm*, *Im3m*, *Ia3d*, *Fm3m*, and *Fd3m*.[25−27] However, the major concern of the soft-templating method comes from utilization or release of hazardous reactants such as formaldehyde and phenol during MC preparation. In fact, formaldehyde is often used as a cross-linking agent in MC synthesis; it is known to be carcinogenic and should be removed from industrial processes. Moreover, phenol is also

carcinogenic and its derivatives are mostly toxic. Even though recent literature reported the successful green manufacturing of a porous carbon fiber monolith by filamentous fungi[28] and macroporous carbon via yeast cells,[29] it still remains a great challenge so far to prepare MC materials by using "friendly" reagents or from a completely green process.

Utilizing biomass (raw resources such as wood or cotton or treated resources including cellulose, lignin, tannin, and starch) as carbon precursor to synthesize MC seems a promising approach. For example, tannin has been utilized as a precursor to synthesize ordered mesoporous carbon through a soft-template method, which still relies on the usage of a soft template.[30] Nanocrystalline cellulose has been used as a precursor to fabricate mesoporous carbon as well.[15] Even though both tannin and cellulose are widely accessible, it is not necessarily a green process to produce them. For example, NaOH (corrosive alkali) treatment is often used to extract the cellulose by removing lignin and hemicellulose from raw materials.[31] To the best of our knowledge, all the reported methods so far rely on the use of certain chemicals to synthesize MC. Without using chemicals, it seems unrealistic to synthesize MC from a bottom-up approach. In this work, a novel top-down approach has been successfully developed to synthesize MC without using any toxic and corrosive chemicals.

EXPERIMENTAL SECTION

Materials. Wood sample was collected from SPF lumber (spruce-pine-fir). Potassium hydroxide (KOH) pellets were purchased from EMD Chemicals. Methylene blue (MB) and methyl orange (MO)

were purchased from Fisher Scientific. *N,N*-Dimethylformamide (DMF) and poly(vinylidene difluoride) (PVDF) were purchased from Sigma−Aldrich. All chemicals were used as received without further treatment.

Preparation of HPTC, a-HPTC, HPTC(r), and a-HPTC(r). Hierarchically porous tubular carbon (HPTC) was prepared in two consecutive thermal treatment steps: carbonization and oxidation. First, raw wood was carbonized in N_2 atmosphere at 800 °C for 2 h with a heating rate of 5 °C/min. Then the carbonized wood (c-wood) was further oxidized in air at 350 °C for 3 h with a heating rate of 5 °C/min. To obtain a-HPTC, 1.0 g HPTC was dispersed in 40 mL (0.25 g/mL) of KOH aqueous solution; the mixture was stirred at 80 °C for 4 h and then kept in static for 20 h. After being dried at 120 °C for 12 h, the mixture was then heated at 700 °C for 2 h with a heating rate of 20 °C/min in nitrogen atmosphere. After cooling down to room temperature, the mixture was washed and filtered with deionized (DI) water until the rinsing water ws neutral and then dried again at 120 °C for 12 h to obtain a-HPTC. Both HPTC and a-HPTC were annealed in N_2 atmosphere at 800 °C for 2 h, and the products were named HPTC(r) and a-HPTC(r).

Characterization. Thermal stability of raw wood and c-wood was studied by thermogravimetric analysis (TGA; TA Instruments Q500) in air atmosphere from 20 to 800 °C with a ramp rate of 10 °C/min. The morphology of c-wood, HPTC, and a-HPTC were characterized by scanning electron microscopy (SEM, JEOL-7401). Transmission electron microscopy (TEM) images of HPTC and a-HPTC were obtained by JEOL JEM-1230 microscope operated at 120 kV. Samples for TEM observation were prepared by drying a drop of sample powder ethanol suspension on carbon-coated copper TEM grids. X-ray photoelectron spectroscopy (XPS) was accomplished by use of a PHI VersaProbe II scanning XPS microprobe with Al $K\alpha$ line excitation source. Brunauer−Emmett−Teller (BET) surface area analysis of samples was performed on a TriStar II 3020 surface analyzer (Micromeritics Instrument Corp.) by N_2 adsorption−desorption isotherms. A UV-1601 Shimadzu spectrophotometer was used to determine the dye concentration in adsorption tests. The surface potential of HPTC and a-HPTC in neutral deionized water was measured by Zetasizer Nano-ZS90 (Malvern).

Adsorption Test. Isotherm adsorption was performed to determine the adsorption capacity. Specifically, 0.5 g/L HPTC and a-HPTC were used to treat 10 mL of MB and MO solutions with different initial concentrations for 12 h. For kinetic studies, 0.5 g/L HPTC and a-HPTC were used to treat 50 mL of 50 ppm MB or MO solutions. For HPTC, 2.0 mL mixtures were collected and filtered for UV−vis tests at 1, 3, 5, 7, 10, 15, and 30 min. Due to the faster adsorption nature, sample collection time was every 30 s up to 5 min for a-HPTC.

Electrochemical Test. The electrochemical properties of the samples were tested with a three-electrode configuration on a VersaSTAT 4 electrochemical workstation (Princeton Applied Research). The working electrode was prepared by mixing 85 wt % active component and 15 wt % PVDF. A drop of DMF was added into the mixture and ground into paste. The paste was dropped onto precleaned Ni foam and then dried at 100 °C for 12 h in a vacuum oven to ensure binding between active material and Ni foam. In the electrochemical test, Pt wire was used as counter electrode and saturated calomel electrode was used as reference. The working electrode was soaked in 6.0 M KOH electrolyte overnight before the test. Cyclic voltammograms (CV) were recorded at different scanning rates of 2, 5, 10, 20, and 50 mV/s in the potential range of −0.8 to 0 V, while charge−discharge tests were conducted at different current densities of 0.2, 0.5, 1, 2, and 5 A/g. Electrochemical impedance spectroscopy (EIS) tests were performed by use of a sinusoidal signal with mean voltage of 0 V and amplitude of 10 mV over a frequency range of 1 000 000−0.01 Hz. Cycling retention was recorded with cycle number up to 5000.

■ RESULTS AND DISCUSSION

Taking a closer look at the structural beauty of natural wood, the basic skeletal substance of the wood cell wall, cellulose, in the mature cell is aggregated into units of structure called microfibrils. Cellulose aggregates have an average diameter of 16 nm with elliptical spaces between having a length/width ratio of ~2 and a minor diameter across the ellipse of 5−10 nm.[32] These elliptical spaces constructed by the cellulose/hemicellulose frame will be filled by lignin molecules afterward. If certain methods can be developed to selectively remove the lignin and leave the cellulose/hemicellulose framework behind, a MC structure constructed by carbonized cellulose framework will be possible (Scheme 1). However, there are still a few

Scheme 1. (a) Structure and Chemical Compositions of Raw Wood and (b) Proposed HPTC Structure after Removal of Lignin
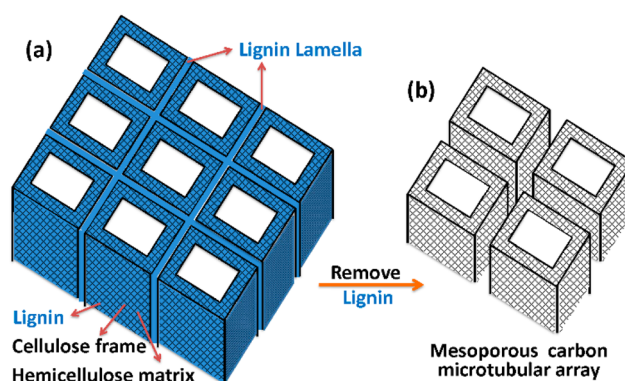
challenges that need to be addressed before this idea can be realized. First of all, it is technically difficult to remove lignin without damaging the cellulose framework by conventional chemical dissolution methods. Acid[33,34] or alkali[35,36] hydrolysis will definitely decrease the molecular weight and crystallinity of cellulose and hemicellulose and thus lead to cellulose structure breakdown. Second, even if the cellulose porous framework remains after chemical treatment, the framework robustness will be an issue during carbonization at elevated temperature. Therefore, the cellulose framework needs to be solidified before any procedures are performed to remove lignin. In this work, a carbonization process is first performed on SPF wood at 800 °C in N_2 atmosphere to give a product named c-wood, which converts both cellulose/hemicellulose framework and filled lignin into carbon, named c-carbon and l-carbon, respectively. HPTC can be obtained by selectively removing the relatively volatile component l-carbon via a chemical-free thermal oxidation approach (Scheme 1). After that, HPTC was further chemically activated with KOH to obtain a-HPTC.

Thermogravimetric analysis was conducted on raw wood and c-wood in air at a heating rate of 10 °C/min (Figure 1). Figure 1a shows the thermogravimetric (TG) and differential thermogravimetric (DTG) curves of raw wood that gives two major degradation peaks (T_{peak}) at 332 and 441 °C, corresponding to the degradation of cellulose and lignin, respectively. The 109 °C higher degradation temperature of lignin is primarily due to its larger molecular weight than that of cellulose, as well as its thermally stable aromatic structure.[37] Generally, hemicelluloses are of much lower molecular weight than cellulose, and thus a broadened shoulder is observed at the left side of the first DTG peak. The weight loss of 58.5 and 36.6
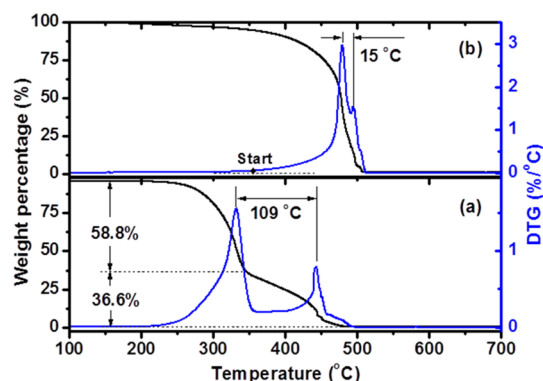
Figure 1. TGA and DTG curves of (a) raw wood and (b) carbonized wood.

wt % in each stage corresponds well to mass fractions of cellulose/hemicellulose and lignin in natural wood. In c-wood, two partially overlapped T_{peak} at 480 and 495 °C are observed, representing the degradation of l-carbon and c-carbon, respectively. Because of the amorphous nature of lignin, l-carbon degrades at lower temperature than c-carbon, which will be further confirmed by following programmed TGA and microstructure study. Even though the two T_{peak} are close to each other, the slight difference in between provides room to remove relatively volatile l-carbon by simple oxidation in air. By heating at the starting decomposition temperature of l-carbon at 350 °C for 3 h, 35% of l-carbon was successfully removed from c-wood (Figure S1, Supporting Information). The weight loss fraction is consistent with the lignin composition in natural wood,[37] which confirms the decomposition of l-carbon at relatively lower temperature.

The microstructure of c-wood before and after thermal oxidation at 350 °C was characterized by SEM and TEM (Figure 2). The tubular cell structure is maintained after
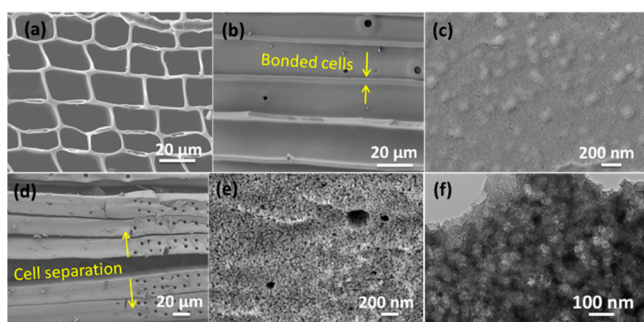

Figure 2. SEM of (a) top view of c-wood, (b) side view of c-wood, (c) enlarged magnification of c-wood side view, (d) side view of HPTC, (e) enlarged magnification of panel d focusing on the surface, and (f) TEM of HPTC showing well-distributed pores in HPTC.

carbonization at 800 °C and all the cells are closely adhered to each other (Figure 2a). Side view of the c-wood in Figure 2b reveals its solid structure with a few micrometer-sized pores. These pores are inherent in the structure of natural wood for intercell mass transportation. The magnified side-view of c-wood shows pore-free surface texture with distributed convex particles of size 50−100 nm, known collectively as the warty layer (lignin-like structure;[38] Figure 2c). After thermal oxidation in air at 350 °C for 3 h, the tubular cells are separated from each other (Figure 2d), which is attributed to

the degradation of lignin "glue" between the cells. This result again confirms the degradation of l-carbon earlier than c-carbon in the TGA study (Figure 1b). More importantly, porous structure was observed on the wall of the tubular cell due to removal of l-carbon (Figure 2e). The TEM image in Figure 2f clearly shows the penetrating pore structure through the cell wall rather than only on the surface, which is essential to achieve large surface area. Focusing on the surface of HPTC, a three-dimensional interwoven nanofibrous structure is observed, reflecting the cellulose skeleton structure in wood (Figure S2, Supporting Information). After activation by KOH, the fibrous structure becomes more closely packed to form smaller pore structures (Figure S3, Supporting Information). Due to the interconnecting nature of the pore structure, it is difficult to determine the pore size from TEM. Therefore, N_2 adsorption−desorption isotherm was performed on HPTC and a-HPTC to determine their pore size and surface area.

Figure 3 shows the typical type IV curves for both HPTC and a-HPTC.[39,40] The hysteresis loop of a-HPTC closed at
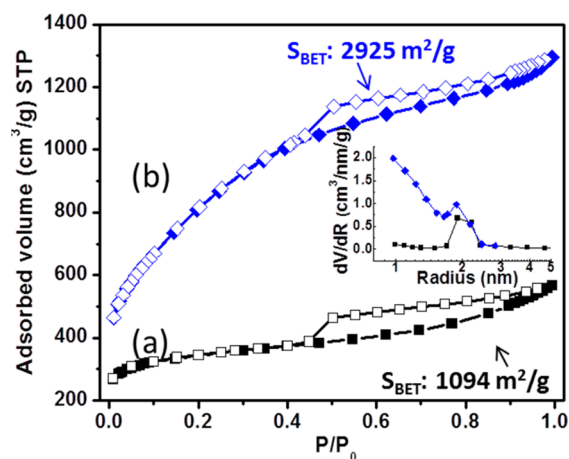
Figure 3. Nitrogen isotherm of (a) HPTC and (b) a-HPTC at 77 K. (Inset) Pore size distribution based on BJH desorption.

lower relative pressure due to the enhanced pore connectivity after activation.[41] The Barrett−Joyner−Halenda (BJH) pore size distribution curves are presented as an inset in Figure 3. Apparently, both HPTC and a-HPTC show narrow pore size distribution with a radius of ~2.0 nm. Chemical activation generates smaller micropores in a-HPTC, evidenced by the uplifted curve shoulder below 2 nm. Therefore, smaller average pore radius of 1.5 nm is obtained in a-HPTC than that of 2.4 nm in HPTC. The BET surface area of HPTC and a-HPTC reaches 1094 and 2925 m^2/g, respectively, which is significantly higher than most of the commercially available activated carbon and template-synthesized mesoporous carbons.[19,42−44]

Besides the larger surface area, thermal oxidation and activation change the surface property significantly. XPS study reveals that the total fraction of oxygen-containing groups (C−O, C=O, and O−C=O) increases from 14.08% (c-wood) to 19.59% and 20.15% after oxidation (HPTC) and activation (a-HPTC), respectively (refer to Figure S4 and Table S1, Supporting Information). The enriched surface oxygen-containing groups play an essential role in adsorption, which is demonstrated in the following adsorption study with organic dye molecules as adsorbate.

The adsorption capacities of both HPTC and a-HPTC with methylene blue (MB) and methyl orange (MO) have been
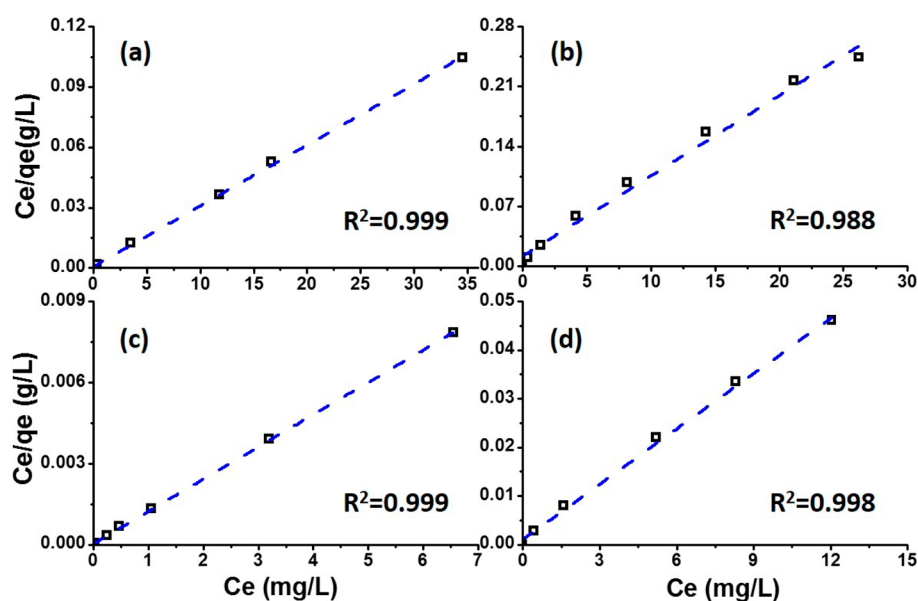
Figure 4. Isothermal adsorption of (a) HPTC−MB, (b) HPTC−MO, (c) a-HPTC−MB, and (d) a-HPTC−MO, fitted with the Langmuir model.
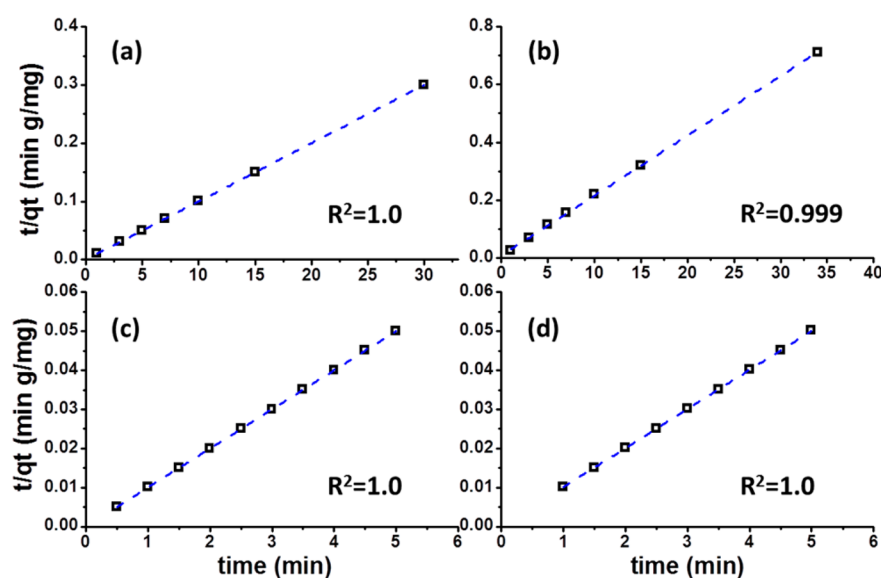

Figure 5. Translated kinetic adsorption t/q_t vs t plots of (a) HPTC−MB, (b) HPTC−MO, (c) a-HPTC−MB, and (d) a-HPTC−MO, fitted with pseudo-second-order model. Initial concentration of MB and MO is 50 ppm.

tested by isotherm adsorption at room temperature (Figure 4). The C_e/q_e versus C_e plots are highly linear with correlation factors (R^2) larger than 0.98. C_e is dye concentration in the remaining solution (milligrams per liter) at equilibrium, and q_e is the amount of dye adsorbed onto adsorbent (milligrams per gram) at equilibrium. The isotherm adsorption results are fitted to the Langmuir isotherm model in eq 1:[45]

$$\frac{C_e}{q_e} = \frac{1}{bq_0} + \frac{C_e}{q_0}$$

(1)

where q_0 is the adsorption capacity (milligrams per gram) of adsorbent and b is the Langmuir adsorption constant related to the binding energy of the adsorption (liters per milligram). q_0 and b can be determined from the slope and intercept in a linear fitted C_e/q_e versus C_e plot. From the Langmuir model, the adsorption capacity of HPTC for MB and MO is calculated as 331 and 109 mg/g (c-wood shows adsorption capacitance of

6 and 4 mg/g for MB and MO, respectively). After further activation, a-HPTC shows ultrahigh adsorption capacity of 838 and 264 mg/g for MB and MO, respectively. To the best of our knowledge, this is the highest MB adsorption capacity that has been achieved in carbon-based materials. Both HPTC and a-HPTC show about 2 times larger capacity in MB adsorption than that of MO, which is attributed to the electrostatic attraction between positively charge MB molecules and negatively charged adsorbent surface. The surface potential of HPTC and a-HPTC is measured as −31.7 and −31.4 mV. The strong interaction between MB and adsorbent is further demonstrated by the larger b value of 5.05 and 52.94 for HPTC and a-HPTC, respectively, while b values for MO on HPTC and a-HPTC are only 0.79 and 4.33, indicating weak adorbate/adsorbent interaction.

To quantify the adsorption rate, kinetic adsorption at room temperature was performed with both HPTC and a-HPTC.

Table 1. Regression Results from Pseudo-Second-Order Kinetic Model

	MB			MO		
	q_e (mg·g^{-1})	K_{ad} (g·mg^{-1}·min^{-1})	h (mg·g^{-1}·min^{-1})	q_e (mg·g^{-1})	K_{ad} (g·mg^{-1}·min^{-1})	h (mg·g^{-1}·min^{-1})
HPTC	100.0	0.896	8963.78	48.3	0.046	108.58
a-HPTC	100.0	1.949	19493.18	100.1	0.667	6680.03

The kinetic results were then fit with different kinetic models including pseudo-first-order,[46] pseudo-second-order,[47,48] Elovich,[49,50] and interparticle diffusion.[51] The formulas and parameters of the four kinetic models are provided in Table S2 (Supporting Information). The correlation coefficient (R^2) is used to evaluate the suitability of each model: a higher R^2 value indicates a more applicable model. Among these models, pseudo-second-order acquires the highest R^2, which can be expressed in eq 2:

$$\frac{t}{qt} = \frac{1}{k_{ad}q_e^2} + \frac{t}{q_e} \qquad (2)$$

where q_t (milligrams per gram) is the solid-phase loading of dye in adsorbent at time t (minutes), q_e (milligrams per gram) is the adsorption capacity at equilibrium, k_{ad} (grams per milligram per minute) is the rate constant of adsorption, and h (milligrams per gram per minute) is the initial adsorption rate at t approaching zero, $h = k_{ad}q_e^2$. The transformed t/q_t versus t plots are highly linear with R^2 values approaching or equal to 1 (Figure 5), indicating a good fit with the pseudo-second-order model. Regression results are summarized in Table 1. The lower q_e value than that of q_0 obtained from the isotherm study is due to diffusion-restricted adsorption in the micropore area within a short time of 30 min. By comparing the ratio of q_e/q_0 (100/331) = 0.30 and $S_{external}/S_{total}$ (341/1094) = 0.31 for MB on HPTC adsorbent, it is surprising to find a highly consistent relationship between each other. That indicates the adsorption primarily occurred at the external surface (including mesopore surface) rather than the micropore surface within the time limited kinetic adsorption process. The adsorption in micropore surface would occur upon extending adsorption time. For example, the adsorption capacity reaches 331 mg/g with 12 h adsorption in the isotherm study. The lower q_e value for MO on HPTC is attributed to the extremely low adsorption rate of 0.046 g·mg^{-1}·min^{-1}. After activation, a-HPTC shows doubled and 13.5 times higher rate constant in MB and MO adsorption as compared to HPTC, indicating the adsorbate uptake is less restricted by the adsorption rate. Thus, similar q_e values of 100.0 and 100.1 g·mg^{-1}·min^{-1} were observed. However, the BET results indicate 4.7 times larger external surface area after activation, which actually does not change q_e in a similar linearly increased manner. These results again confirm that the enhanced surface area after activation is primarily created by the newly formed micropores, where dye adsorption is kinetically restricted in a limited adsorption time.

The MB adsorption capacity against BET surface area has been plotted in Figure 6, which summarizes the MB adsorption capacity by using carbon-based adsorbents from literature reports (open symbols) and materials tested in this study (arrow-marked solid symbols). With commercial activated carbon (HDB M-1951, Cabot Corp.) as a reference, HPTC shows 29.7% enhancement in MB adsorption capacity. After activation, a-HPTC exhibits the highest surface area and largest MB adsorption capacity among all the reported materials. By this simple method, a-HPTC achieves 2−5 times larger surface
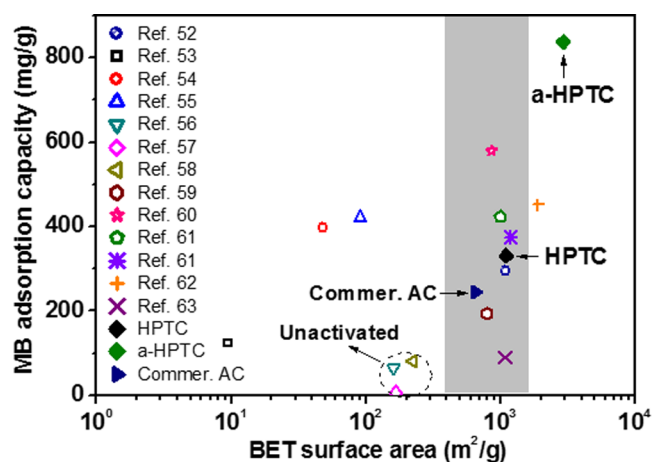

Figure 6. Plot of MB adsorption capacity against BET surface area of materials from current study and literature reports.[52−62] The gray shaded area indicates the typical surface area range of porous carbon from template methods.

area than template-synthesized mesoporous carbon, as marked by the gray shaded area in Figure 6. Apparently, it is not necessarily true that larger surface area leads to larger MB adsorption capacity. For example, activated carbon prepared from rattan sawdust[63] has ∼100 times larger surface area than that of dehydrated wheat bran carbon,[53] yet it shows even lower MB adsorption capacity (Figure 6). All these results reveal that not only specific surface area but also pore size and surface properties contribute to the final adsorption property. The ultrahigh surface area of a-HPTC together with its abundant surface functional groups ensure an extremely large adsorption capacity in this study.

Besides the unprecedented organic dye adsorption capacity, these materials also show very promising electrochemical energy storage properties (Figure 7). CV curves of HPTC, HPTC(r), a-HPTC, and a-HPTC(r) are plotted in Figure 7a. Typically, a CV curve getting close to square shape indicates better energy storage properties. Moreover, the capacitance value is linearly related to the circled area of CV loop. Therefore, it can be concluded that the energy storage performance of a-HPTC and a-HPTC(r) is significantly better than that of HPTC and HPTC(r). The quantified capacitance results at different voltage scan rates are summarized in Figure 7b, where a-HPTC(r) shows the greatest rate performance with capacitance drops from 222.5 to 138.8 F/g with increasing scan rate from 2 to 50 mV/s. The capacitance is larger than most of the reported carbon materials, such as activated graphene (∼166 F/g at discharge current density of 1.4 A/g),[64] CNT/graphene (125 F/g at 10 mV/s),[65] and nanodiamond/graphene (143 F/g at discharge current density 0.2 A/g).[66] Even though a-HPTC gives the highest capacitance of 246.4 F/g at 2 mV/s, it drops to 55.2 F/g while the scan rate increases to 50 mV/s. Overall, the capacitance can be significantly improved by both activation and reduction. It is worth mentioning that the reduction process does not change the surface area significantly
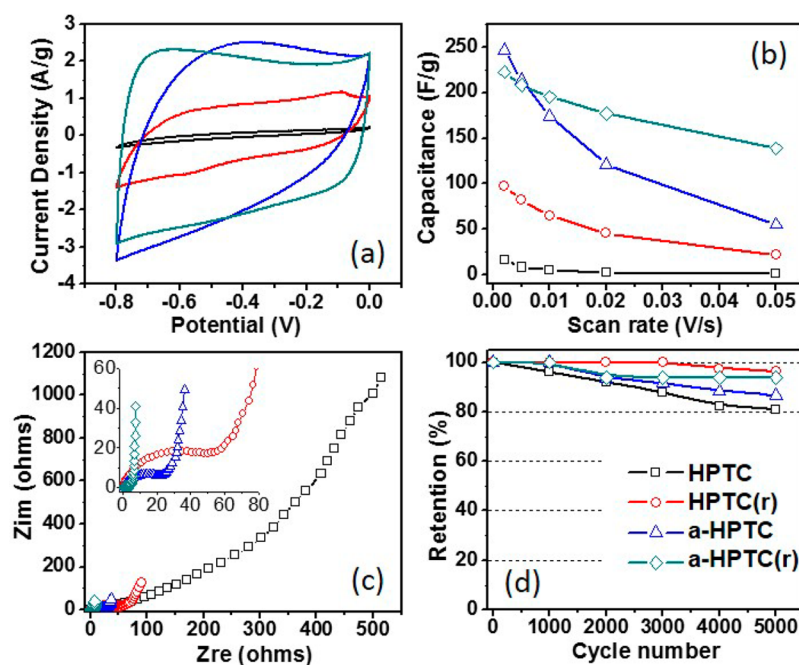
Figure 7. (a) CV at scan rate of 10 mV/s, (b) capacitance vs scan rate, (c) EIS, and (d) cycling retention over 5000 cycles by use of HPTC, HPTC(r), a-HPTC, and a-HPTC(r) as electrodes. c-wood shows a capacitance of <10 F/g within the voltage scan rate 2−50 mV/s.

(Figure S5, Supporting Information). The specific surface area of HPTC(r) and a-HPTC(r) is measured as 1028 and 2836 m^2/g, which is slightly smaller than the values before reduction, probably due to the collapse of weak pore structures during annealing. However, the slight surface area change could not be the reason for the significant change in electrochemical capacitance.

Activation generates larger surface area and it is positively related to the area of the electric double layer, where electrical energy is stored. By reduction in N_2, the electrical conductivity of the carbon can be enhanced (via reduced polarization resistance) for efficient electron transfer during charge/discharge. Therefore, a-HPTC(r) exhibit the best energy storage performance among the four materials. The impedance spectra for HPTC(r), a-HPTC, and a-HPTC(r) in Figure 7c is composed of a partial semicircle at high frequency followed by a linear part at low frequency, signifying typical capacitive behavior. The smaller semicircle diameter represents smaller polarization resistance of the specific electrode, which is beneficial to the enhancement of energy storage properties. Cycling test over 5000 cycles shows good long-term stability of the reduced samples, HPTC(r) and a-HPTC(r), with over 90% retention, while the unreduced samples still show 80% retention (Figure 7d).

CONCLUSION

In summary, we report a template-free approach to synthesize mesoporous carbon hollow tubes by using natural wood as carbon precursor. Large surface area of 1094 m^2/g can be achieved by thermal treatment alone, without introduction of any chemicals. Moreover, the surface area increases to 2925 m^2/g after KOH activation. These porous carbons with ultrahigh surface area show outstanding organic dye adsorption properties (MB and MO), and an unprecedented high adsorption capacity of 838 mg/g has been achieved with MB adsorbate. After thermal reduction, the porous carbon could serve as a supercapacitor electrode for electrochemical energy

storage, and a capacity of larger than 200 F/g was achieved. This simple method can be applied to process large surface area carbon from other similar biomass such as bamboo and hard wood. With the advantage of the hierarchical microtube/mesopore feature, these materials could find wider applications in adsorption, energy storage/conversion, and catalysis.

ASSOCIATED CONTENT

$\textbf{S}$ Supporting Information

Five figures and three tables with additional characterization results including TGA, SEM, TEM, and XPS. The Supporting Information is available free of charge on the ACS Publications website at DOI: 10.1021/acsami.5b02697.

AUTHOR INFORMATION

Corresponding Author
*E-mail jzhu1@uakron.edu; fax (330) 972-5856; phone (330) 972-6859.

Notes
The authors declare no competing financial interest.

ACKNOWLEDGMENTS

REFERENCES

(1) Zhao, Y.; Ran, W.; He, J.; Song, Y.; Zhang, C.; Xiong, D.-B.; Gao, F.; Wu, J.; Xia, Y. Oxygen-rich hierarchical porous carbon derived from artemia cyst shells with superior electrochemical performance. *ACS Appl. Mater. Interfaces* **2015**, *7* (2), 1132−1139.

(2) Hao, G.-P.; Jin, Z.-Y.; Sun, Q.; Zhang, X.-Q.; Zhang, J.-T.; Lu, A.-H. Porous carbon nanosheets with precisely tunable thickness and selective CO_2 adsorption properties. *Energy Environ. Sci.* **2013**, *6* (12), 3740−3747.

(3) Ben, T.; Li, Y.; Zhu, L.; Zhang, D.; Cao, D.; Xiang, Z.; Yao, X.; Qiu, S. Selective adsorption of carbon dioxide by carbonized porous aromatic framework (PAF). *Energy Environ. Sci.* **2012**, *5* (8), 8370−8376.

(4) Merlet, C.; Rotenberg, B.; Madden, P. A.; Taberna, P.-L.; Simon, P.; Gogotsi, Y.; Salanne, M. On the molecular origin of super-capacitance in nanoporous carbon electrodes. *Nat. Mater.* **2012**, *11* (4), 306−310.

(5) Hao, G.-P.; Li, W.-C.; Qian, D.; Lu, A.-H. Rapid synthesis of nitrogen-doped porous carbon monolith for CO_2 capture. *Adv. Mater.* **2010**, *22* (7), 853−857.

(6) Hao, G.-P.; Li, W.-C.; Qian, D.; Wang, G.-H.; Zhang, W.-P.; Zhang, T.; Wang, A.-Q.; Schüth, F.; Bongard, H.-J.; Lu, A.-H. Structurally designed synthesis of mechanically stable poly-(benzoxazine-co-resol)-based porous carbon monoliths and their application as high-performance CO_2 capture sorbents. *J. Am. Chem. Soc.* **2011**, *133* (29), 11378−11388.

(7) Zhai, Y.; Dou, Y.; Zhao, D.; Fulvio, P. F.; Mayes, R. T.; Dai, S. Carbon materials for chemical capacitive energy storage. *Adv. Mater.* **2011**, *23* (42), 4828−4850.

(8) He, X.; Male, K. B.; Nesterenko, P. N.; Brabazon, D.; Paull, B.; Luong, J. H. T. Adsorption and desorption of methylene blue on porous carbon monoliths and nanocrystalline cellulose. *ACS Appl. Mater. Interfaces* **2013**, *5* (17), 8796−8804.

(9) You, B.; Jiang, J.; Fan, S. Three-dimensional hierarchically porous all-carbon foams for supercapacitor. *ACS Appl. Mater. Interfaces* **2014**, *6* (17), 15302−15308.

(10) Sevilla, M.; Parra, J. B.; Fuertes, A. B. Assessment of the role of micropore size and N-doping in CO_2 capture by porous carbons. *ACS Appl. Mater. Interfaces* **2013**, *5* (13), 6360−6368.

(11) Vinu, A.; Ariga, K.; Mori, T.; Nakanishi, T.; Hishita, S.; Golberg, D.; Bando, Y. Preparation and characterization of well-ordered hexagonal mesoporous carbon nitride. *Adv. Mater.* **2005**, *17* (13), 1648−1652.

(12) Mane, G. P.; Talapaneni, S. N.; Anand, C.; Varghese, S.; Iwai, H.; Ji, Q.; Ariga, K.; Mori, T.; Vinu, A. Preparation of highly ordered nitrogen-containing mesoporous carbon from a gelatin biomolecule and its excellent sensing of acetic acid. *Adv. Funct. Mater.* **2012**, *22* (17), 3596−3604.

(13) Liang, C.; Li, Z.; Dai, S. Mesoporous carbon materials: Synthesis and modification. *Angew. Chem., Int. Ed.* **2008**, *47* (20), 3696−3717.

(14) Böttger-Hiller, F.; Kempe, P.; Cox, G.; Panchenko, A.; Janssen, N.; Petzold, A.; Thurn-Albrecht, T.; Borchardt, L.; Rose, M.; Kaskel, S.; Georgi, C.; Lang, H.; Spange, S. Twin polymerization at spherical hard templates: An approach to size-adjustable carbon hollow spheres with micro- or mesoporous shells. *Angew. Chem., Int. Ed.* **2013**, *52* (23), 6088−6091.

(15) Shopsowitz, K. E.; Hamad, W. Y.; MacLachlan, M. J. Chiral nematic mesoporous carbon derived from nanocrystalline cellulose. *Angew. Chem., Int. Ed.* **2011**, *50* (46), 10991−10995.

(16) Li, X.; Cao, Y.; Qi, W.; Saraf, L. V.; Xiao, J.; Nie, Z.; Mietek, J.; Zhang, J.-G.; Schwenzer, B.; Liu, J. Optimization of mesoporous carbon structures for lithium-sulfur battery applications. *J. Mater. Chem.* **2011**, *21* (41), 16603−16610.

(17) Cai, J.; Li, L.; Lv, X.; Yang, C.; Zhao, X. Large surface area ordered porous carbons via nanocasting zeolite 10x and high performance for hydrogen storage application. *ACS Appl. Mater. Interfaces* **2014**, *6* (1), 167−175.

(18) Kubo, S.; Tan, I.; White, R. J.; Antonietti, M.; Titirici, M.-M. Template synthesis of carbonaceous tubular nanostructures with tunable surface properties. *Chem. Mater.* **2010**, *22* (24), 6590−6597.

(19) Zhai, Y.; Dou, Y.; Liu, X.; Park, S. S.; Ha, C.-S.; Zhao, D. Soft-template synthesis of ordered mesoporous carbon/nanoparticle nickel composites with a high surface area. *Carbon* **2011**, *49* (2), 545−555.

(20) Guo, B.; Wang, X.; Fulvio, P. F.; Chi, M.; Mahurin, S. M.; Sun, X.-G.; Dai, S. Soft-templated mesoporous carbon-carbon nanotube composites for high performance lithium-ion batteries. *Adv. Mater.* **2011**, *23* (40), 4661−4666.

(21) Li, H.-Q.; Liu, R.-L.; Zhao, D.-Y.; Xia, Y.-Y. Electrochemical properties of an ordered mesoporous carbon prepared by direct tri-constituent co-assembly. *Carbon* **2007**, *45* (13), 2628−2635.

(22) Fang, Y.; Gu, D.; Zou, Y.; Wu, Z.; Li, F.; Che, R.; Deng, Y.; Tu, B.; Zhao, D.; Low-Concentration, A. Hydrothermal synthesis of biocompatible ordered mesoporous carbon nanospheres with tunable and uniform size. *Angew. Chem., Int. Ed.* **2010**, *49* (43), 7987−7991.

(23) Gencoglu, M. F.; Spurri, A.; Franko, M.; Chen, J.; Hensley, D. K.; Heldt, C. L.; Saha, D. Biocompatibility of soft-templated mesoporous carbons. *ACS Appl. Mater. Interfaces* **2014**, *6* (17), 15068−15077.

(24) Liang, C.; Hong, K.; Guiochon, G. A.; Mays, J. W.; Dai, S. Synthesis of a large-scale highly ordered porous carbon film by self-assembly of block copolymers. *Angew. Chem., Int. Ed.* **2004**, *43* (43), 5785−5789.

(25) Meng, Y.; Gu, D.; Zhang, F.; Shi, Y.; Cheng, L.; Feng, D.; Wu, Z.; Chen, Z.; Wan, Y.; Stein, A.; Zhao, D. A family of highly ordered mesoporous polymer resin and carbon structures from organic−organic self-assembly. *Chem. Mater.* **2006**, *18* (18), 4447−4464.

(26) Song, L.; Feng, D.; Fredin, N. J.; Yager, K. G.; Jones, R. L.; Wu, Q.; Zhao, D.; Vogt, B. D. Challenges in fabrication of mesoporous carbon films with ordered cylindrical pores via phenolic oligomer self-assembly with triblock copolymers. *ACS Nano* **2009**, *4* (1), 189−198.

(27) Tanaka, S.; Nishiyama, N.; Egashira, Y.; Ueyama, K. Synthesis of ordered mesoporous carbons with channel structure from an organic-organic nanocomposite. *Chem. Commun.* **2005**, *16*, 2125−2127.

(28) Zhang, L.; Wang, Y.; Peng, B.; Yu, W.; Wang, H.; Wang, T.; Deng, B.; Chai, L.; Zhang, K.; Wang, J. Preparation of a macroscopic, robust carbon-fiber monolith from filamentous fungi and its application in Li-S batteries. *Green Chem.* **2014**, *16* (8), 3926−3934.

(29) Sun, H.; He, W.; Zong, C.; Lu, L. Template-free synthesis of renewable macroporous carbon via yeast cells for high-performance supercapacitor electrode materials. *ACS Appl. Mater. Interfaces* **2013**, *5* (6), 2261−2268.

(30) Schlienger, S.; Graff, A.-L.; Celzard, A.; Parmentier, J. Direct synthesis of ordered mesoporous polymer and carbon materials by a biosourced precursor. *Green Chem.* **2012**, *14* (2), 313−316.

(31) Johar, N.; Ahmad, I.; Dufresne, A. Extraction, preparation and characterization of cellulose fibres and nanocrystals from rice husk. *Ind. Crops Prod.* **2012**, *37* (1), 93−99.

(32) Salmen, L.; Olsson, A.-M.; Stevanic, H. S.; Simonovic, J.; Rasotic, K. Structural organization of the wood polymers in the wood fiber structure. *Bioresources* **2012**, *7*, 521−532.

(33) Sannigrahi, P.; Ragauskas, A.; Miller, S. Effects of two-stage dilute acid pretreatment on the structure and composition of lignin and cellulose in loblolly pine. *BioEnergy Res.* **2008**, *1* (3−4), 205−214.

(34) Marzialetti, T.; Valenzuela Olarte, M. B.; Sievers, C.; Hoskins, T. J. C.; Agrawal, P. K.; Jones, C. W. Dilute acid hydrolysis of loblolly pine: A comprehensive approach. *Ind. Eng. Chem. Res.* **2008**, *47* (19), 7131−7140.

(35) Carrillo, F.; Lis, M. J.; Colom, X.; López-Mesas, M.; Valldeperas, J. Effect of alkali pretreatment on cellulase hydrolysis of wheat straw: Kinetic study. *Process Biochem.* **2005**, *40* (10), 3360−3364.

(36) Karuna, N.; Zhang, L.; Walton, J. H.; Couturier, M.; Oztop, M. H.; Master, E. R.; McCarthy, M. J.; Jeoh, T. The impact of alkali pretreatment and post-pretreatment conditioning on the surface properties of rice straw affecting cellulose accessibility to cellulases. *Bioresour. Technol.* **2014**, *167*, 232−240.

(37) Shafizadeh, F. The chemistry of pyrolysis and combustion. In *The Chemistry of Solid Wood*; Rowell, R., Ed.; Advances in Chemistry Series, Vol. *207*; American Chemical Society: Washington, DC, 1984; Chapt. 13, pp 489−529.

(38) Wilfred, A., Jr. *Cellular Ultrastructure of Woody Plants*; Syracuse University Press: Syracuse, NY, 1965.

(39) Kruk, M.; Jaroniec, M. Gas adsorption characterization of ordered organic−inorganic nanocomposite materials. *Chem. Mater.* **2001**, *13* (10), 3169−3183.

(40) Fulvio, P. F.; Mayes, R. T.; Wang, X.; Mahurin, S. M.; Bauer, J. C.; Presser, V.; McDonough, J.; Gogotsi, Y.; Dai, S. Brick-and-mortar

self-assembly approach to graphitic mesoporous carbon nano-composites. *Adv. Funct. Mater.* **2011**, *21* (12), 2208−2215.

(41) Ball, P. C.; Evans, R. Temperature dependence of gas adsorption on a mesoporous solid: Capillary criticality and hysteresis. *Langmuir* **1989**, *5* (3), 714−723.

(42) Górka, J.; Zawislak, A.; Choma, J.; Jaroniec, M. KOH activation of mesoporous carbons obtained by soft-templating. *Carbon* **2008**, *46* (8), 1159−1161.

(43) Ramasamy, E.; Chun, J.; Lee, J. Soft-template synthesized ordered mesoporous carbon counter electrodes for dye-sensitized solar cells. *Carbon* **2010**, *48* (15), 4563−4565.

(44) Ryoo, R.; Joo, S. H.; Kruk, M.; Jaroniec, M. Ordered mesoporous carbons. *Adv. Mater.* **2001**, *13* (9), 677−681.

(45) Langmuir, I. The adsorption of gases on plane surfaces of glass, mica, and platinum. *J. Am. Chem. Soc.* **1918**, *40* (9), 1361−1403.

(46) Ho, Y. S.; McKay, G. Sorption of dye from aqueous solution by peat. *Chem. Eng. J.* **1998**, *70* (2), 115−124.

(47) Ho, Y. S.; McKay, G.; Wase, D. A. J.; Forster, C. F. Study of the sorption of divalent metal ions on to peat. *Adsorpt. Sci. Technol.* **2000**, *18*, 639−650.

(48) Zhu, J.; Gu, H.; Guo, J.; Chen, M.; Wei, H.; Luo, Z.; Colorado, H. A.; Yerra, N.; Ding, D.; Ho, T. C.; Haldolaarachchige, N.; Hopper, J.; Young, D. P.; Guo, Z.; Wei, S. Mesoporous magnetic carbon nanocomposite fabrics for highly efficient Cr(VI) removal. *J. Mater. Chem. A* **2014**, *2* (7), 2256−2265.

(49) Juang, R.-S.; Chen, M.-L. Application of the Elovich equation to the kinetics of metal sorption with solvent-impregnated resins. *Ind. Eng. Chem. Res.* **1997**, *36* (3), 813−820.

(50) Sparks, D. L. Kinetics of reaction in pure and mixed systems. In *Soil Physical Chemistry*; CRC Press: Boca Raton, FL, 1986; pp 83−145.

(51) Srivastava, S. K.; Tyagi, R.; Pant, N. Adsorption of heavy metal ions on carbonaceous material developed from the waste slurry generated in local fertilizer plants. *Water Res.* **1989**, *23* (9), 1161−1165.

(52) Hameed, B. H.; Ahmad, A. L.; Latiff, K. N. A. Adsorption of basic dye (methylene blue) onto activated carbon prepared from rattan sawdust. *Dyes Pigm.* **2007**, *75* (1), 143−149.

(53) Özer, A.; Dursun, G. Removal of methylene blue from aqueous solution by dehydrated wheat bran carbon. *J. Hazard. Mater.* **2007**, *146* (1−2), 262−269.

(54) Liu, F.; Chung, S.; Oh, G.; Seo, T. S. Three-dimensional graphene oxide nanostructure for fast and efficient water-soluble dye removal. *ACS Appl. Mater. Interfaces* **2011**, *4* (2), 922−927.

(55) Barton, S. S. The adsorption of methylene blue by active carbon. *Carbon* **1987**, *25* (3), 343−350.

(56) Yao, Y.; Xu, F.; Chen, M.; Xu, Z.; Zhu, Z. Adsorption behavior of methylene blue on carbon nanotubes. *Bioresour. Technol.* **2010**, *101* (9), 3040−3046.

(57) Kavitha, D.; Namasivayam, C. Experimental and kinetic studies on methylene blue adsorption by coir pith carbon. *Bioresour. Technol.* **2007**, *98* (1), 14−21.

(58) Wang, S.; Li, L.; Wu, H.; Zhu, Z. H. Unburned carbon as a low-cost adsorbent for treatment of methylene blue-containing wastewater. *J. Colloid Interface Sci.* **2005**, *292* (2), 336−343.

(59) Deng, H.; Yang, L.; Tao, G.; Dai, J. Preparation and characterization of activated carbon from cotton stalk by microwave assisted chemical activation: Application in methylene blue adsorption from aqueous solution. *J. Hazard. Mater.* **2009**, *166* (2−3), 1514−1521.

(60) El Qada, E. N.; Allen, S. J.; Walker, G. M. Adsorption of methylene blue onto activated carbon produced from steam activated bituminous coal: A study of equilibrium adsorption isotherm. *Chem. Eng. J.* **2006**, *124* (1−3), 103−110.

(61) Altenor, S.; Carene, B.; Emmanuel, E.; Lambert, J.; Ehrhardt, J.-J.; Gaspard, S. Adsorption studies of methylene blue and phenol onto vetiver roots activated carbon prepared by chemical activation. *J. Hazard. Mater.* **2009**, *165* (1−3), 1029−1039.

(62) Hameed, B. H.; Din, A. T. M.; Ahmad, A. L. Adsorption of methylene blue onto bamboo-based activated carbon: Kinetics and equilibrium studies. *J. Hazard. Mater.* **2007**, *141* (3), 819−825.

(63) Ahmad, A. L.; Loh, M. M.; Aziz, J. A. Preparation and characterization of activated carbon from oil palm wood and its evaluation on methylene blue adsorption. *Dyes Pigm.* **2007**, *75* (2), 263−272.

(64) Zhu, Y.; Murali, S.; Stoller, M. D.; Ganesh, K. J.; Cai, W.; Ferreira, P. J.; Pirkle, A.; Wallace, R. M.; Cychosz, K. A.; Thommes, M.; Su, D.; Stach, E. A.; Ruoff, R. S. Carbon-based supercapacitors produced by activation of graphene. *Science* **2011**, *332* (6037), 1537−1541.

(65) Yu, D.; Dai, L. Self-assembled graphene/carbon nanotube hybrid films for supercapacitors. *J. Phys. Chem. Lett.* **2009**, *1* (2), 467−470.

(66) Sun, Y.; Wu, Q.; Xu, Y.; Bai, H.; Li, C.; Shi, G. Highly conductive and flexible mesoporous graphitic films prepared by graphitizing the composites of graphene oxide and nanodiamond. *J. Mater. Chem.* **2011**, *21* (20), 7154−7160.